Crystal Structure of Oxidized *Bacillus pasteurii* Cytochrome c_{553} at 0.97-Å Resolution[†]

Stefano Benini,[‡] Ana González,[‡] Wojciech R. Rypniewski,*[,‡] Keith S. Wilson,[§] Jozef J. Van Beeumen,[‖] and Stefano Ciurli*[,⊥]

European Molecular Biology Laboratory, c/o DESY, Notkestrasse 85, D-22603 Hamburg, Germany, Department of Chemistry, University of York, Heslington, York, YO10 5DD, United Kingdom, Laboratorium voor Eiwitbiochemie en Eiwitengineering, University of Gent, Ledeganckstraat 35, 9000 Gent, Belgium, and Department of Agro-Environmental Science and Technology, University of Bologna, Viale Berti Pichat 10 I-40127 Bologna, Italy

ABSTRACT: This article reports the first X-ray structure of the soluble form of a *c*-type cytochrome isolated from a Gram-positive bacterium. *Bacillus pasteurii* cytochrome c_{553}, characterized by a low reduction potential and by a low sequence homology with cytochromes from Gram-negative bacteria or eukaryotes, is a useful case study for understanding the structure−function relationships for this class of electron-transfer proteins. Diffraction data on a single crystal of cytochrome c_{553} were obtained using synchrotron radiation at 100 K. The structure was determined at 0.97-Å resolution using ab initio phasing and independently at 1.70 Å in an MAD experiment. In both experiments, the structure solution exploited the presence of a single Fe atom as anomalous scatterer in the protein. For the 0.97-Å data, the phasing was based on a single data set. This is the most precise structure of a heme protein to date. The crystallized cytochrome c_{553} contains only 71 of the 92 residues expected from the intact protein sequence, lacking the first 21 amino acids at the N-terminus. This feature is consistent with previous evidence that this tail, responsible for anchoring the protein to the cytoplasm membrane, is easily cleaved off during the purification procedure. The heme prosthetic group in *B. pasteurii* cytochrome c_{553} is surrounded by three α-helices in a compact arrangement. The largely exposed c-type heme group features a His−Met axial coordination of the Fe(III) ion. The protein is characterized by a very asymmetric charge distribution, with the exposed heme edge located on a surface patch devoid of net charges. A structural search of a representative set of protein structures reveals that *B. pasteurii* cytochrome c_{553} is most similar to *Pseudomonas* cytochromes c_{551}, followed by cytochromes c_6, *Desulfovibrio* cytochrome c_{553}, cytochromes c_{552} from thermophiles, and cytochromes *c* from eukaryotes. Notwithstanding a low sequence homology, a structure-based alignment of these cytochromes shows conservation of three helical regions, with different additional secondary structure motifs characterizing each protein. In *B. pasteurii* cytochrome c_{553}, these motifs are represented by the shortest interhelix connecting fragments observed for this group of proteins. The possible relationships between heme solvent accessibility and the electrochemical reduction potential are discussed.

Bacillus species are Gram-positive microorganisms lacking a true periplasm and are obliged to store electron-transfer proteins as membrane-bound forms. Three types of class I *c*-type cytochromes have been identified in Gram-positive bacteria: (i) cytochromes fused as integral domains of subunit II in membrane-bound aa_3-type terminal oxidases, (ii) cytochromes bound to the membrane through an N-terminal hydrophobic polypeptide, and (iii) cytochromes bound to the membrane via a diacyl−glyceryl−cysteine moiety (*1*). The difficulties associated with the study of such water-insoluble proteins may explain why only a few *c*-type cytochromes have been isolated from Gram-positive bacteria (*2−13*). As a consequence, their properties and functional roles are scarcely known, and no structural information is available, in contrast with cytochromes from Gram-negative bacteria and eukaryotes (*14*, *15*).

The Gram-positive alkaliphilic soil bacterium *Bacillus pasteurii* produces large amounts of membrane-bound cytochromes of the b- and c-types, as well as a terminal oxidase of the aa_3-type (*16*, *17*). Recently, the soluble form of a *c*-type cytochrome (named cytochrome c_{553}) has been purified (*12*). *B. pasteurii* cytochrome c_{553} is a small (9.6 kDa) acidic (p*I* = 3.3) protein (*12*), having a chain length of 92 amino acids and a single heme-binding sequence pattern (Cys−

* To whom correspondence should be sent. Stefano Ciurli, Department of Agro-Environmental Science and Technology, University of Bologna, Viale Berti Pichat, 10 I-40127 Bologna, Italy; phone: +39-051-2099794; fax: +39-51-243362; e-mail: sciurli@agrsci.unibo.it. Wojciech R. Rypniewski, EMBL, Notkestrasse 85, D-22603 Hamburg, Germany; phone: +49-40-89902142; fax: +49-40-89902149; e-mail: wojtek@embl-hamburg.de.
[‡] European Molecular Biology Laboratory.
[§] University of York.
[‖] University of Gent.
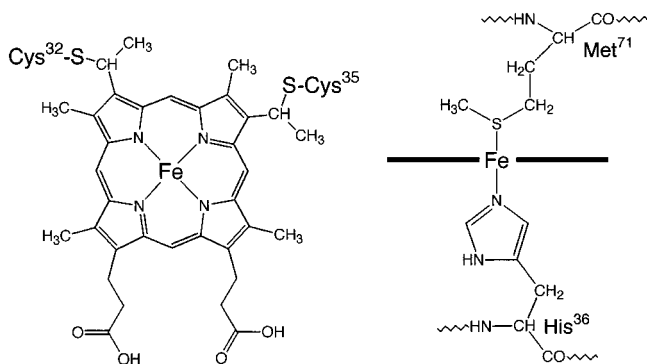[⊥] University of Bologna.

FIGURE 1: Scheme of the heme prosthetic group as detected in *B. pasteurii* cytochrome c_{553} by paramagnetic NMR spectroscopy (*20*). Top and side views are shown.

X–X–Cys–His) located in the first half of the polypeptide chain (*18*). These features indicate that the protein belongs to class I cytochromes (*19*). Its amino acid sequence suggests that in vivo cytochrome c_{553} is bound to the cytoplasm membrane through a diacyl–glyceryl–cysteine anchor located at the N-terminus tail and that the soluble form is obtained by cleavage of this tail during cell disruption (*18*). A paramagnetic NMR spectroscopic study on the oxidized Fe(III) form confirmed the presence of a *c*-type heme and additionally allowed the identification of a hexacoordinate low-spin Fe ion axially bound to His and Met residues (Figure 1) (*20*). Direct electrochemical measurements established a low reduction potential ($E^{\circ\prime} = +47$ mV) (*20*), as expected for cytochromes from alkalophiles (*8, 21*). The thermodynamic parameters for the one-electron reduction process suggested that the heme group is highly exposed to the solvent and that extrusion of water molecules from the protein hydration shell occurs upon reduction (*20*). The function of cytochrome c_{553} in *B. pasteurii* is unknown, but it probably plays a role in respiratory metabolism (*18*).

Crystals of cytochrome c_{553} diffracting to atomic resolution were obtained (*12*). The present article reports the refined X-ray structure of *B. pasteurii* cytochrome c_{553}, the first available for cytochromes from Gram-positive bacteria, determined at 0.97-Å resolution using ab initio phasing methods, as well as at 1.70 Å using MAD data.

MATERIALS AND METHODS

Protein Purification and Crystallization. Cells of *B. pasteurii* were grown as reported previously (*22*), and cytochrome c_{553} was purified in the oxidized form, using a described procedure (*12*) slightly modified to separate the observed multiple protein isoforms (*18*). In particular, a gradient of ammonium sulfate solution (2 to 0 M) was used for the hydrophobic interaction chromatography, so that only the major component was isolated in a pure state. Protein crystallization was achieved at 20 °C using the hanging drop method, by mixing 3 μL of a 16 mg/mL protein solution in 20 mM Tris-HCl at pH 8.0, with 3 μL of 100 mM sodium acetate at pH 5.0, containing 3.2 M ammonium sulfate (*12*). The final pH was 5.1. Regularly shaped rods having dimensions of $0.2 \times 0.2 \times 0.6$ mm^3 on average were obtained after one week. *B. pasteurii* cytochrome c_{553} crystallizes in the orthorhombic space group $P2_12_12_1$, with 1 molecule (7.7 kDa) per asymmetric unit. The calculated

volume-to-mass ratio ($V_M = 2.1$ Å^3/Da) and solvent content of the crystal (41%) are in the normal range found for proteins (*23*).

MAD Experiment to Medium Resolution. The multiple anomalous dispersion (MAD) data were collected on a vitrified crystal at 100 K at the EMBL Hamburg outstation wiggler beam line BW7A, using a 180-mm MAR image plate scanner. An X-ray fluorescence spectrum was measured around the Fe K edge using lyophilized protein. An initial diffraction $f\prime$ data set was collected at the inflection point of the absorption edge ($E = 7121$ eV, $\lambda = 1.741$ Å). A second data set was collected almost 30 eV away from the edge ($E = 7146$ eV, $\lambda = 1.735$ Å) to obtain a large $f\prime\prime$ value but minimize the risk of a large loss of anomalous signal in case of wavelength instabilities. A third, remote wavelength ($E = 12\,400$ eV, $\lambda = 0.996$ Å) was selected to maximize the changes in intensities between reflections collected at different wavelength (dispersive differences), which often proves necessary to determine the correct phase unequivocally (*24*). Collection at this wavelength also provided a data set with fewer absorption errors and allowed an increase of the resolution of the data, limited to 2.16 Å near the Fe K edge by the size of the detector. The maximum resolution at the remote wavelength was 1.70 Å. Collection of a full data set with a 90° oscillation was possible because of the orthorhombic symmetry of the crystals (*25*).

All computations were carried out with programs from the CCP4 package (*26*) unless otherwise stated. The data were processed and scaled separately with the HKL package programs DENZO and SCALEPACK (*27*) and subsequently merged using AGROVATA. The unit cell parameters were determined by postrefinement in SCALEPACK, using the 1.70-Å resolution data. All the data were scaled to the data set collected at the remote wavelength using SCALEIT. The final statistics for MAD data collection are summarized in Table 1.

Both the anomalous difference and the dispersive difference Patterson maps clearly showed the Fe site. MLPHARE was used to refine the initial estimate of the Fe position and to calculate an initial set of phases. The overall figure of merit at 2.16-Å resolution was 0.64 for 715 centric and 0.54 for 2744 acentric reflections. Several cycles of solvent modification were carried out using the program DM with the solvent flip option to improve further the quality of the map, initially extending only to 2.16 Å and, after convergence, to 1.70 Å. Both possible structure hands gave very similar statistics, and the correct hand was selected by visual inspection.

The initial map was clearly interpretable, with excellent density for the heme. Electron density maps, ($3F_o–F_c$) and ($F_o–F_c$), were inspected and interpreted with the program O (*28*). The density assignment was carried out automatically with the program ARP (*29*). The program was given the position of the Fe atom and the solvent modified map as input, and it was set to search successively for density peaks at a distance between 1.2 and 2.2 Å from other atoms. These peaks were assigned to oxygen atoms. The process was interrupted after the program found ca. 1200 atoms (the total expected number was approximately 900 atoms for protein and solvent). Subsequently, some unrestrained refinement cycles were done combining SFALL and ARP until the free *R* factor started to decrease. Following this step, unrestrained

Table 1: X-ray Data Collection Statistics and Data Reduction for *B. pasteurii* Cytochrome c_{553}

	MAD			ab initio
	maximum f''	minimum f'	remote	
wavelength (Å)	1.735	1.741	0.996	0.886
lowest resolution (Å)	20	20	20	20
highest resolution (Å)	2.16	2.16	1.70	0.97
no. of images	90	90	90	179
oscillation range (°)	1	1	1	0.8−3.0
% R_{merge} (overall/anomalous)[a]	6.8/5.7	6.8/4.0	4.0/2.7	7.4/na
raw measurements	11 297	70 712	26 088	212 694
unique reflections	3712	3678	7417	38 906
redundancy	3.04	19.22	3.52	5.47
anomalous measurements	2884	2858	6076	34 853
% completeness	99.1	98.4	99.5	99.9
% completeness [high-resolution bin (Å)]	87.8 (2.23−2.16)	87.7 (2.23−2.16)	97.1 (1.76−1.70)	99.6 (0.99−0.97)
% greater than 3 σ	95.2	95.4	93.0	86.3
I/σ in highest resolution bin	3.2 (2.23−2.16)	3.2 (2.23−2.16)	5.4 (1.76−1.70)	4.2 (0.99−0.97)
space group	$P2_12_12_1$	$P2_12_12_1$	$P2_12_12_1$	$P2_12_12_1$
a (Å)	37.1	37.1	37.1	37.1
b (Å)	39.2	39.2	39.2	39.4
c (Å)	44.0	44.0	44.0	44.0

[a] $R_{merge} = \Sigma|I_i - \langle I \rangle|/\Sigma\langle I \rangle$, where I_i is an individual intensity measurement, and $\langle I \rangle$ is the average intensity for this reflection with summation over all the data.

refinement was continued with the maximum likelihood based program REFMAC (*30*).

When the *R* factor decreased to 0.18 and R_{free} decreased to 0.23, a ($3F_o−2F_c$) map was calculated, and the program PEPT (Lamzin, personal communication) was used to automatically trace the protein main chain. The final map showed clearly the side chains and the heme group, thereby allowing the building of the whole protein model. The model was subsequently refined using the standard Engh and Huber geometrical constraints (*31*), turning off the van der Waals radius for the Fe atom. The parameters refined were the atomic position and the isotropic B-factor for each nonhydrogen atom. Positions of hydrogen atoms were calculated before each maximum likelihood refinement cycle, and their contribution to the structure factors was added to the structure factors calculated from the model. After refinement with REFMAC, new atoms were added at density points >3 σ in the ($F_o−F_c$) map. Atoms lying in density <1 σ in ($3F_o−2F_c$) maps, or positioned at less than 1.2 Å from each other, were deleted. The final statistics for the model derived from the MAD data, as well as the stereochemical restraints and the final standard deviations from target values (*31*), are summarized in Table 2.

Atomic Resolution Study. A single crystal of cytochrome c_{553} was used to collect 100 K diffraction data at 0.97 Å, at the BW7B wiggler beam line of the Hamburg EMBL outstation, using radiation of $\lambda = 0.885$ Å and a 30-cm MAR Research imaging plate scanner. The data collection and processing (*12*) are reported in Table 1.

The X-ray wavelength was optimized for collection of atomic resolution data, and no effort was made to maximize the anomalous signal. However, the Patterson map calculated with coefficients $[F(+) − F(−)]^2$ using all data showed a single peak in the Harker sections, at the 8 σ level, corresponding to the anomalous signal from the single iron ion (*12*). Similar maps, calculated using data having a lower resolution cutoff, showed the same peak at successively diminishing levels. A single Fe atom was placed in the unit cell at the position derived from the anomalous Patterson map, setting its van der Waals radius to zero. This position

Table 2: Summary of the Crystallographic Analysis and Refinement for *B. pasteurii* Cytochrome c_{553}

	MAD	ab initio
protein heavy atoms	497	497
hydrogen atoms		486
heme atoms	42	42
solvent atoms	128	125
bound metal ions	1 Fe	1 Fe
overall temperature factors (Å²)	10.9	14.7
temperature factors for main chain (Å²)	5.9	8.7
temperature factors side chain (Å²)	10.0	13.3
temperature factors for solvent (Å²)	25.8	33.4
temperature factors for Fe (Å²)	2.4	5.1
temperature factors for heme (Å²)	4.3	6.9
B-factors from Wilson plot (Å²)	10.0	10.1
r.m.s. on final $F_o−F_c$ map (electrons/Å³)	0.13	0.09
maximum value of the final $F_o−F_c$ map (electrons/Å³)	3.2	0.7
minimum value of the final $F_o−F_c$ map (electrons/Å³)	−0.6	−0.4
Ramachandran most favored region (%)	89.5	89.1
Ramachandran additional allowed region (%)	8.0	9.1
Ramachandran generously allowed region (%)	1.8	1.8
deviation from bond lengths target values[a] (Å)	0.010 (0.020)	0.016 (0.020)
deviation from bond angles target values[a] (Å)	0.027 (0.040)	0.034 (0.040)
deviation from chiral volumes target values[a] (Å³)	0.150 (0.145)	0.117 (0.100)
R factor (R_{free})[b] (%)	0.17 (0.21)	0.12

[a] Standard devations (σ) are in parentheses; the weights for the least-squares refinement correspond to $1/\sigma^2$. [b] R factor $= \Sigma ||F_o| − |F_c||/\Sigma|F_o|$; R factor and R_{free} are calculated by using the working and free reflection sets, respectively; the free reflections (5% of the total) were held aside throughout the refinement.

was used as the starting model in an iterative procedure involving (i) automatic interpretation of electron density maps using the program ARP (*29*) and (ii) cycles of unrestrained refinement of atomic positions and isotropic B-factors, using either a least-squares minimization implemented in the program PROLSQ (*32, 33*) or maximum-likelihood using

REFMAC (*30*). ARP was set up to remove atoms from the model if they were found in density <1 σ in the ($3F_o-2F_c$) map. New atomic positions were selected from peaks showing density >3 σ in the (F_o-F_c) map and lying within 1.1−3.3 Å of existing atoms in the model. Atoms were inserted and refined using ARP with real space positional refinement. Atoms were merged into a single site if the distance between them became less than 1.0 Å. The maximum number of new atoms to find and remove was set to 20 for each cycle in the case of least-squares refinement. In the maximum-likelihood refinement, the number of atoms removed and inserted was not limited. Electron density maps, ($3F_o-2F_c$) and (F_o-F_c), were inspected and interpreted with the program O (*28*).

When the *R* factor fell to approximately 0.18, further refinement was carried out using SHELXL96 (*34*). The model was refined against measured diffraction intensities rather than structure factor amplitudes. This eliminated the problem of dealing with negative intensity measurements for weak data, as no square roots need to be taken. Hydrogen positions were determined either from known, fixed stereo-chemistry or, in for example methyl groups, by the automatic procedure included in SHELXL96 for interpreting the electron density map. Hydrogen positions were recalculated at every cycle. Default restraints for bond lengths, bond angles, and chiral volumes were applied for protein stereo-chemistry. No specific targets were specified for the geom-etry of the heme, the only restraint applied being that chemically equivalent bond distances should be equal. Anisotropic temperature factors were refined for all atoms. Solvent atoms continued to be inserted automatically with the ARP procedure. The relative occupancies of multiple side chain conformations were refined keeping the sum con-strained to unity.

Most of the refinement was performed using the conjugate gradient algorithm, but in the last two cycles, block-matrix least-squares minimization was employed to obtain a direct estimate of errors in coordinates and temperature factors from the covariance matrix. The model was refined in blocks of 20 residues each, with a one-residue overlap between blocks, to decrease the size of the computation. The final statistics for the model derived from ab initio data are summarized in Table 2. The standard uncertainties for all refined parameters were estimated only for the atomic resolution structure, using the covariance matrix in a special cycle of least-squares minimization without restraints or damping. The overall estimated standard uncertainties (esu) for all atomic positions are given in Table 3.

The quality of both models was checked using PROCHECK (*35*) and WHATIF (*36*). The coordinates and derived models have been deposited in the PDB with the accession codes 1C75 (ab initio) and 1B7V (MAD).

RESULTS AND DISCUSSION

Comparison between the MAD and ab Initio Structure Solution. Both ab initio and MAD methodologies can be used for direct phasing of protein structures. One of the main advantages of anomalous dispersion methods, as compared to multiple isomorphous replacement (MIR), is that they only require one heavy atom species to solve the phase determi-nation problem and that the species can be part of the native

Table 3: Overall Estimated Standard Uncertainties (esu) for the Atomic Positions (Å) of the ab Initio [a] *B. pasteurii* Cytochrome c_{553} Model

overall	0.051
protein	0.040
carbon	0.041
nitrogen	0.039
oxygen	0.039
sulfur	0.004
solvent	0.085
main chain	0.024
carbon	0.028
nitrogen	0.023
oxygen	0.017
heme	0.014
carbon	0.015
nitrogen	0.010
oxygen	0.013
Fe	0.002

[a] For the 1.7-Å MAD model, the overall estimated standard uncertainties for the coordinates was 0.12 Å, based on *R* factor, and 0.11 Å, based on R_{free}.

protein (*37−40*). This avoids or minimizes the amount of time necessary to prepare heavy atom derivatives. The only restrictions on the feasibility of MAD experiments are (i) having an absorption edge of the anomalous scatterer within the X-ray spectrum available from protein crystallography beam lines at synchrotrons and (ii) a sufficiently large anomalous signal. In contrast, ab initio methods are so far restricted to crystals diffracting to very high resolution (1.2 Å or better) or else to cases in which there is one or more heavy atoms in the sample (*41*). Such methods represent a very attractive solution to the phase problem because they require only one data set.

Both phasing methods are applicable to the structural determination of metallo-proteins, as they can take advantage of the presence of the heavy atom. For *B. pasteurii* cytochrome c_{553}, this is represented by the heme iron ion. Using MAD, a high anomalous/nonanomalous scatterer ratio is obtained yielding a large mean anomalous signal (3.6%). For ab initio methods, a single strong peak in the Patterson map corresponding to the anomalous signal from the single iron ion can be observed even without optimization of the anomalous signal (*12*).

The feasibility and reliability of both methods can be appreciated by comparing the two final models of *B. pasteurii* cytochrome c_{553} obtained after the two independent structure determinations and refinements. The difference between the two final models is very low: the RMSD for the coordinates is 0.074 Å for the Cα atoms (with maximum displacement 0.145 Å) and 0.073 Å for all main chain atoms (maximum displacement 0.225 Å). The following description of the structure, unless stated otherwise, refers to the atomic resolution structure determined by ab initio methods.

The Overall Fold of Cytochrome c_{553}. Both structural models of *B. pasteurii* cytochrome c_{553} contain only 71 of the 92 residues expected from the intact protein sequence (*18*). The peptide chain starts with Val22, clearly revealing the absence of the N-terminus tail detected by amino acid sequence analysis and supposed to be responsible for anchoring the protein to the cytoplasm membrane of this Gram-positive bacterium. This observation indicates that such an N-terminus is easily hydrolyzed upon protein purification, as also previously suggested (*18*).
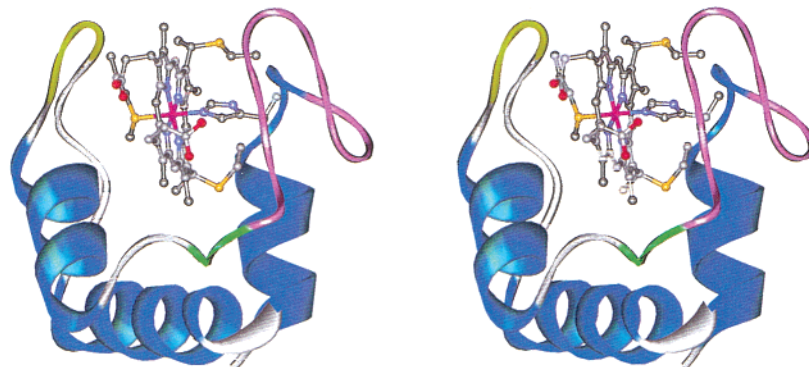
FIGURE 2: Stereoview of the ribbon plot of *B. pasteurii* cytochrome c_{553}. The heme prosthetic group and the heme coordinating residues are presented as a ball-and-stick model colored according to the atom type. The ribbon is colored according to the secondary structure (blue: helices; green: 3_{10} helix; purple: Ω-loop; yellow: β-turn-β motif.

A single protein chain folds around the heme (Figure 2), and includes three α-helices, a short 3_{10} helix, and several turns and connecting random coil fragments, accounting for 47.9, 4.2, 25.4, and 22.6% of the total 71 residues, as determined by DSSP (*42*). The α-helical regions correspond to those predicted by the program PREDATOR (*43*) using only the amino acid sequence (*18*).

Overall, the tertiary structure is quite compact, without disordered and extended loops. The N-terminal helix (Ala24 to His36) is bent, with the first segment covering residues Ala24−Lys31, followed by a kink involving Cys32 and a short helical fragment (Ile33−His36). The N-terminal helix contains three residues involved in the enclosure of the heme prosthetic group within the protein matrix: Cys32 and Cys35 are covalently bound to the heme, while His36 is one of the two axial ligands to the heme Fe atom.

The N-terminus helix is followed by a Ω-shaped loop involving a type I reverse turn (Gly37−Lys40), a sharp turn (Ala43−Ala45), and a second type I reverse turn (Ile48−Ala51). The sharp turn is stabilized by an H-bond between Ala43 NH and Ala45 O, with the Ser44 side chain extending from the tip of the turn. In addition to this intraturn interaction, an additional H-bond between Ala45 NH and the heme-bound Cys35 O is observed, directly linking the conformation of the Ω loop to the position of the heme group.

The Ω loop is followed by a short 3_{10} helix (Ala51−Ala53), by a four-residue β-hairpin (Gly52−Tyr55), and by a longer (middle) helix (Glu57−Asn66). A short two-stranded antiparallel β-sheet, formed by only two interchain H-bonds between Gln68 and Met71, as well as by a type-II′ β-turn including Gly69 and Gly70, further contributes to enveloping the heme group through the coordination between Met71 Sδ and the Fe ion.

The subsequent peptide segment (Pro72−Lys77) is devoid of any inter- or intrachain H-bonds but is stabilized in the observed conformation by the presence of a rigidly positioned solvent molecule (W95, B = 9.7 Å^2). This water donates two H-bonds to the carbonyl atoms of Ile64 (belonging to the central helix) and Pro72, while receiving an H-bond from Ile75 NH. W95 is the only buried solvent molecule in the protein matrix and is shielded from contact with bulk solvent by a small hydrophobic region (Pro72−Gly73−Gly74−Ile75−Ala76) belonging to the peptide fragment connecting Met50 to the C-terminus helix.

The sequence ends with the C-terminal helix (Gly78−Ala89), which stabilizes the overall protein fold through close contacts (3.6−3.8 Å) with all other helical fragments, involving hydrophobic interactions. These contacts include (i) the side chain of Trp87 and Val84 (C-terminal helix) and of Ala24 and Val27−Val28, respectively (N-terminal helix), (ii) the side chains of Ala81, Val84, Ala85, Ala86, and Ala89 (C-terminal helix) on one side and those of Glu57, Ile60, Leu61, Ile64, and Leu65 (middle helix) on the other, and (iii) the Ala89 backbone atoms (C-terminal helix) and Gly52 Cα (3_{10} helix). Further stabilization of these interactions is provided by the salt bridge between Glu80 Oϵ1 (C-terminal helix) and Lys31 Nζ (N-terminal helix) and the H-bond between Leu88 O (C-terminal helix) and Gly52 NH (middle helix).

Peptide Conformation. The dihedral angles ϕ and ψ display very similar distributions for both atomic resolution and MAD models. All residues lie within the favored regions, the only outlier being Ala43 ($\phi = -147°$, $\psi = -112°$). Inspection of the electron density around this residue confirmed that the density is well-defined and that Ala43 is modeled correctly. Its unusual conformation, although sterically unfavorable, probably results from the need to satisfy some other structural requirement. Ala43 is part of the sharp turn on the Ω-loop flanking the heme on the side of His36. Changing ψ of Ala43 would affect the dihedral angles for the neighboring Ser44, which is in a favorable conformation ($\phi = -65°$, $\psi = -33°$) at the tip of the sharp turn. Decreasing ψ for this residue would also bring Ala43 O into close contact with Ala45 O (they are 3.6 Å apart). In contrast, changing ϕ would affect the hydrogen bond between Ala43 NH and Ala45 O that is fundamental to maintaining the conformation of the turn and of the overall Ω-loop.

Large deviations from planarity (up to 20°) of peptide bonds are observed for both the atomic resolution and the MAD models, in keeping with previous observations (*44*). The deviations are highly significant for the atomic resolution structure, with standard deviations of approximately 1°. There is an excellent correlation (R = 0.93) of the ω angles between the 0.97-Å and the 1.70-Å structures, indicating that reliable information about the nonplanarity of peptide bonds is available even in structures obtained at lower than atomic resolution. It is therefore important that too tight planarity restraints are not imposed during refinement.
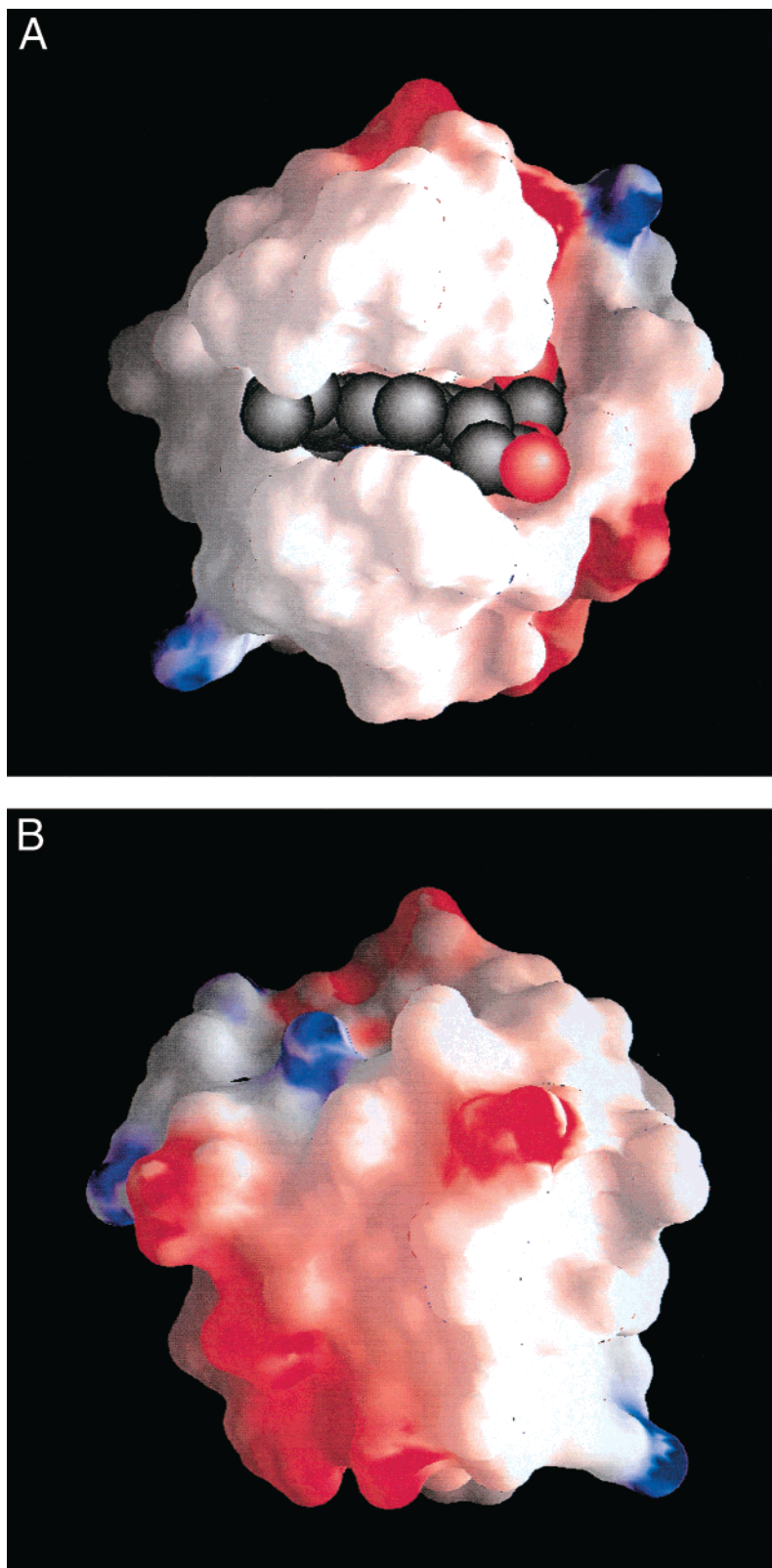
FIGURE 3: Solid surface representation of the electrostatic potential of *B. pasteurii* cytochrome c_{553}. The molecular surface and electrostatic mapping were generated by the program GRASP (*73*), using a probe radius of 1.4 Å. The electrostatic potential was calculated using a simple version of a Poisson−Boltzmann solver, with the GRASP full charge set, and the heme group was excluded from the calculations. Dielectric constants of 80 and 2 were used for the solvent and protein interior, respectively. The surface is colored according to the calculated electrostatic potential contoured from -10 kT/e (intense red) to $+10$ kT/e (intense blue). The heme group atoms are represented as a spheres, colored according to the CPK color scheme. The protein is shown with the heme crevice toward the viewer (panel A) and rotated by 180° about a vertical axis (panel B).

Surface Electrostatic Potential. The surface potential map of *B. pasteurii* cytochrome c_{553} (Figure 3) indicates that the protein is characterized by a highly asymmetric charge distribution. The surface surrounding the heme group, devoid of net charges, constitutes a distinct hydrophobic area, while most charges are located on the opposite side of the exposed

FIGURE 4: (A) "Top" view of the atomic model of the heme group in *B. pasteurii* cytochrome c_{553}, superimposed on the final $3F_o-2F_c$ elec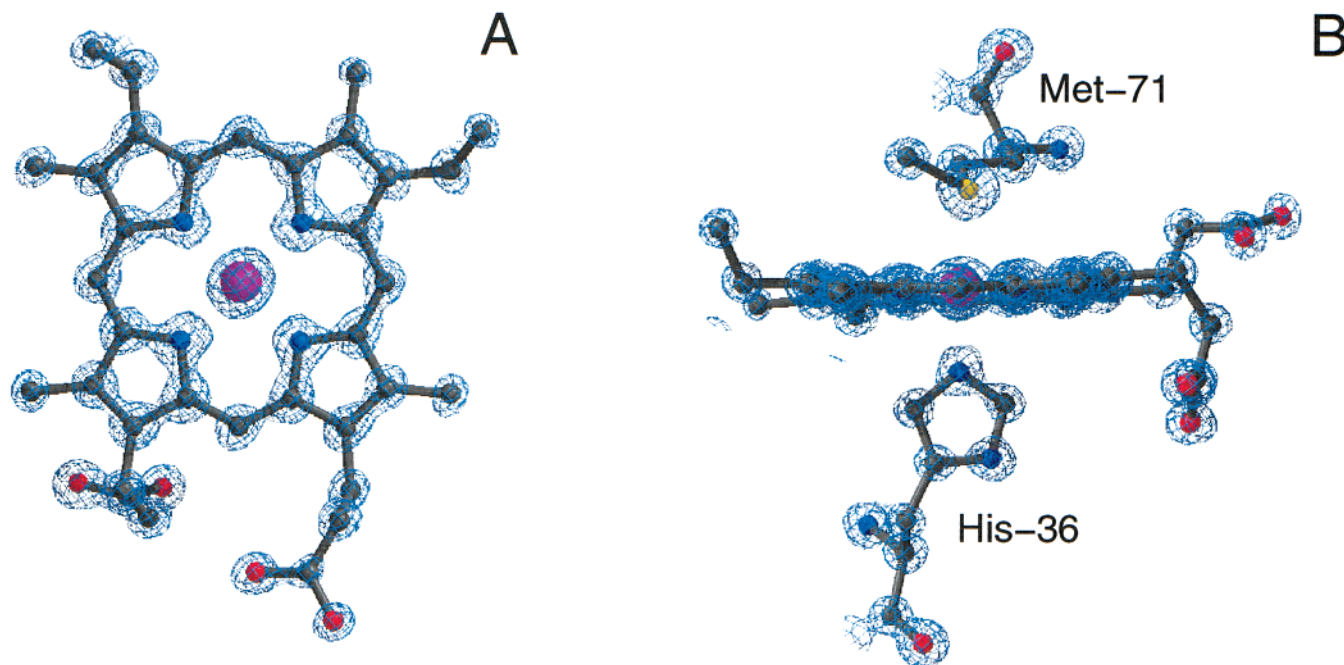tron density map; (B) "side view" of the same model. Atoms are colored according to atom type. The side chains of Cys32 and Cys35, as well as the axial residues in panel A, are not shown for clarity. Figures made using BOBSCRIPT (*74*).

heme edge. A similar charge distribution has been observed in cytochromes c_6 (*45−48*) as well as in cytochromes c_{552} from thermophiles (*49, 50*). In contrast, a positively charged front surface, formed by several lysine residues grouped around the solvent-exposed edge of heme pyrrole C, is found in cytochromes *c* and c_2 (*51−54*), as well as in *Desulfovibrio vulgaris* cytochrome c_{553} (*55*). The surface area surrounding the heme crevice is generally considered to represent the site for molecular recognition during electron transfer.

The Heme Prosthetic Group. The $3F_o-2F_c$ electron density map of the heme group is shown in Figure 4. The structure of the heme group (Figure 1) is in agreement with the NMR data previously reported (*20*). The heme group is close to planar (RMSD from the plane = 0.08 Å), with the Fe(III) ion in an octahedral coordination geometry. The equatorial ligands are the four nitrogen atoms of the heme pyrrole groups, while the axial ligands are His36 Nϵ and Met71 Sδ. The geometric properties of the Fe atom (Table 4) are statistically equivalent to the model obtained by MAD. These metric features are not significantly different from those observed in all other crystallographically determined cytochrome structures, regardless of the oxidation state of the Fe ion. The much lower precision of the structures of cytochromes reported so far allows neither a statistically significant comparison of the heme iron coordination geometry nor a redox-state-dependent comparison of these properties. The nitrogen atoms of the pyrrole rings are in close contact with His 36 Nϵ (2.86, 2.79, 2.78, and 2.79 Å), and Met71 Sδ (2.93, 3.11, 3.20, and 3.02 Å). These distances are short by standard definitions of van der Waals radii: it appears that the radii of the pyrrole ring nitrogen atoms are reduced, probably due to the electron density being partially drawn toward the iron.

The heme is covalently bound to the protein matrix through two thioether bonds, between the Cys32 and the Cys35 Sγ atoms and the heme Cα atoms at positions 2 and 4,

Table 4: Selected Distances and Angles around the Fe Atom in *Bacillus pasteurii* Cytochrome c_{553}

Fe−L distances (Å)	ab initio	MAD
Fe−His15 Nϵ	1.99	2.0
Fe−Met50 Sγ	2.332	2.3
Fe−N$_A$	2.00	2.0
Fe−N$_B$	1.98	2.0
Fe−N$_C$	1.99	2.0
Fe−N$_D$	1.97	2.0

L−Fe−L angles (°)	ab initio	MAD
N$_A$−Fe−N$_B$	90.2	90
N$_B$−Fe−N$_C$	89.4	90
N$_C$−Fe−N$_D$	89.9	89
N$_D$−Fe−N$_A$	90.4	90
His15 Nϵ−Fe−N$_A$	91.4	88
His15 Nϵ−Fe−N$_B$	89.4	91
His15 Nϵ−Fe−N$_C$	88.3	91
His15 Nϵ−Fe−N$_D$	89.7	88
Met50 Sγ−Fe−N$_A$	85.0	85
Met50 Sγ−Fe−N$_B$	92.2	91
Met50 Sγ−Fe−N$_C$	95.3	95
Met50 Sγ−Fe−N$_D$	88.7	90
Met50 Sγ−Fe−His15 Nϵ	176.0	174

respectively. A hydrogen bond is donated by His36 NHδ to the peptide carbonyl oxygen of a nearby residue (Pro46), a feature common to all cytochromes. The heme is sandwiched between two hydrophobic patches: on the methionine face, one patch is composed of the side chains of Ile63, Ile64, Pro72, and Ile75, in addition to Met71 itself, whereas on the histidine face another patch is made up of Ser34, Ala45, Pro46, and Ile48, in addition to the side chains of Cys32 and Cys35. The innermost portion of the heme group (pyrrole ring A) is close to the hydrophobic chains of Val84 and Leu88. This hydrophobic cavity is a common feature of all cytochromes. The peptide chain folds around the heme leaving the edge of pyrrole rings B, C, and D very exposed to solvent (Figures 2 and 3).
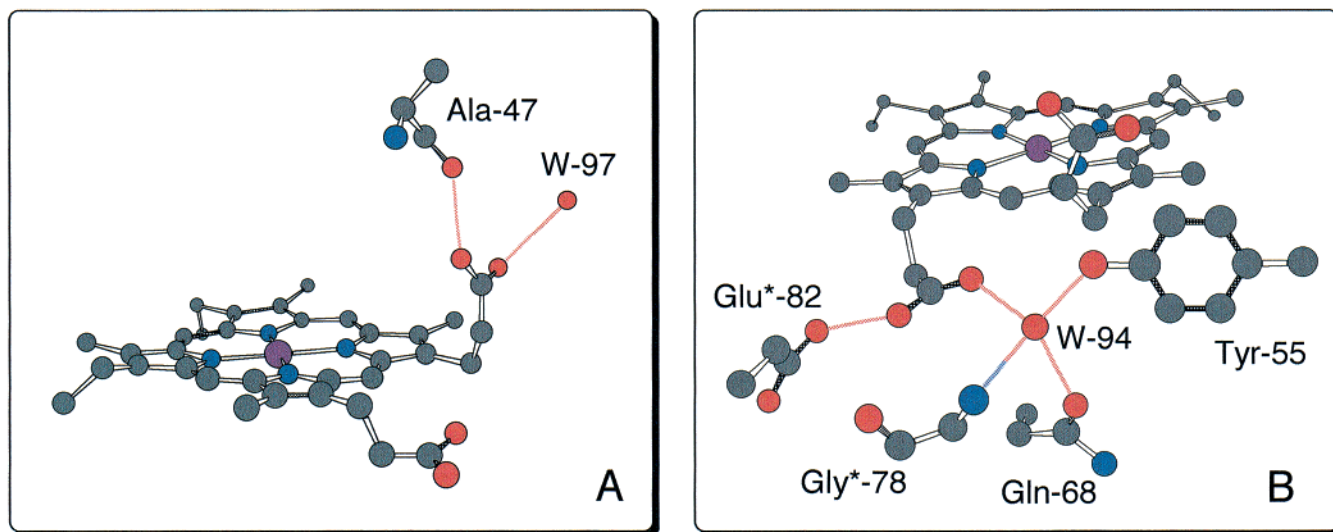
FIGURE 5: Scheme of the H-bonding networks around the heme propionate-7 (A) and propionate-6 (B). H-bonds are colored according to the color of the atoms involved. Hydrogen atoms are not shown. Residues belonging to adjacent molecules in the crystal are labeled with asterisks.

Both heme propionate chains are clearly defined in the electron density maps. Propionate-6 extends toward the protein exterior, while propionate-7 is bent toward the protein inner matrix (see Figures 2−4). Although no hydrogen atom density is visible, the accuracy of the structure allows an assignment of the protonation state of the propionate carboxylic groups on the basis of the C−O distances, as well as of the observed H-bonding patterns.

A strong H-bond [at 2.64(4) Å] is formed between the main chain carbonyl oxygen of Ala47 and heme propionate-7 $O\delta 1$ (Figure 5, panel A), indicating that the latter is protonated. The presence of a proton on propionate-7 $O\delta 1$ is consistent with a $C\gamma-O\delta 1$ distance of 1.29(2) Å, statistically equivalent to the canonical value of 1.30 Å for the C−OH distance in a neutral carboxylic group (*31*). Furthermore, this distance is significantly longer than the C−O distance for a charged carboxylate moiety (1.23 Å) (*31*). In contrast, the propionate-7 $C\gamma-O\delta 2$ distance is 1.25(2) Å, close to the expected value (1.21 Å) for a C=O double bond (*31*). This distance is slightly larger than expected, probably because of a strong H-bond [2.80(9) Å] formed between propionate-7 $O\delta 2$ and a solvent molecule (W97, Figure 5, panel A).

In the heme propionate-6 side chain, the $C\gamma-O\delta$ distances are equivalent [1.26(2) and 1.27(2) Å], suggesting that this group is deprotonated. There is a strong H-bond between propionate-6 $O\delta 1$ and Glu82 $O\epsilon 2$ from a neighboring molecule [at 2.50(4) Å, Figure 5, panel B], a residue characterized by equivalent $C\delta-O\epsilon 1$ and $C\delta-O\epsilon 2$ distances [1.25(2) and 1.27(2) Å, respectively]. The proton involved in this H-bond is therefore equally shared between the two oxygen atoms. In solution, the interaction with Glu82 $O\epsilon 2$ would be lost, leaving a propionate-6 moiety probably H-bonded to a water molecule through its $O\delta 1$ atom. Propionate-6 $O\delta 2$ is H-bonded [2.74(8) Å] to a well-ordered ($B = 9.2$ Å^2) solvent molecule (W94). W94 is situated at the center of a tetrahedral H-bonding network involving Tyr55 $O\eta$ [2.72(9) Å], Gln68 $O\epsilon 1$ [2.77(5) Å], and Gly78 N from a neighboring molecule [2.87(5) Å], in addition to heme propionate-6 $O\delta 2$ (Figure 5, panel B). The chemical

nature and geometry of this configuration suggests that the lone pairs of the water molecule are directed toward Tyr55 $O\eta H$ and the symmetry-related Gly78 NH, while the protons are presented to Gln68 $O\epsilon$ and to the propionate-6 $O\delta 2$. In solution, the interaction of W94 with the symmetry-related Gly78 NH would be absent, and this water would make an H-bond with another solvent molecule.

Eukaryotic cytochromes, such as those from horse heart (*56*), rat (*57*), and yeast (*58, 59*) contain a well-ordered conserved water molecule in the vicinity of the heme propionate groups, in a position similar but not equivalent to that of W94 in *B. pasteurii* cytochrome c_{553}. In *Saccharomyces cerevisiae* iso-1-cytochrome, this water is involved in an H-bonding network with Asn52, Tyr67, and Thr78, three residues that are not conserved in *B. pasteurii* cytochrome c_{553}. Movement of the conserved water molecule has been proposed to regulate the redox-dependent thermal stability of yeast iso-1-cytochrome (*59*). However, algae cytochromes c_6 also contain a single, well-ordered water molecule positioned between the two propionate moieties of the heme (*45, 48*), but its position is not affected by redox processes (*48*). Therefore, a general assignment for a structural and/or functional role of well-ordered water molecules in *c*-type cytochromes is not yet possible.

In conclusion, this analysis indicates that, at the crystallization pH of 5.1, propionate-7 is protonated and neutral. A previous study of the physicochemical properties of *B. pasteurii* cytochrome c_{553} revealed that both NMR and electrochemical parameters depended on pH, with a transition occurring at pH 5.5 (*20*). The data suggested that such pH modulation involves heme propionate-7. The present structural investigation supports this hypothesis and further suggests that the deprotonation of propionate-7, occurring at higher pH, disrupts the H-bond with Ala-47 O, probably leading to a major conformational change. To elucidate this point, we are currently determining the structure of *B. pasteurii* cytochrome c_{553} at pH 7 in solution, using NMR spectroscopy.

Comparison with Other Cytochromes. The amino acid sequence of *B. pasteurii* cytochrome c_{553} is most similar to
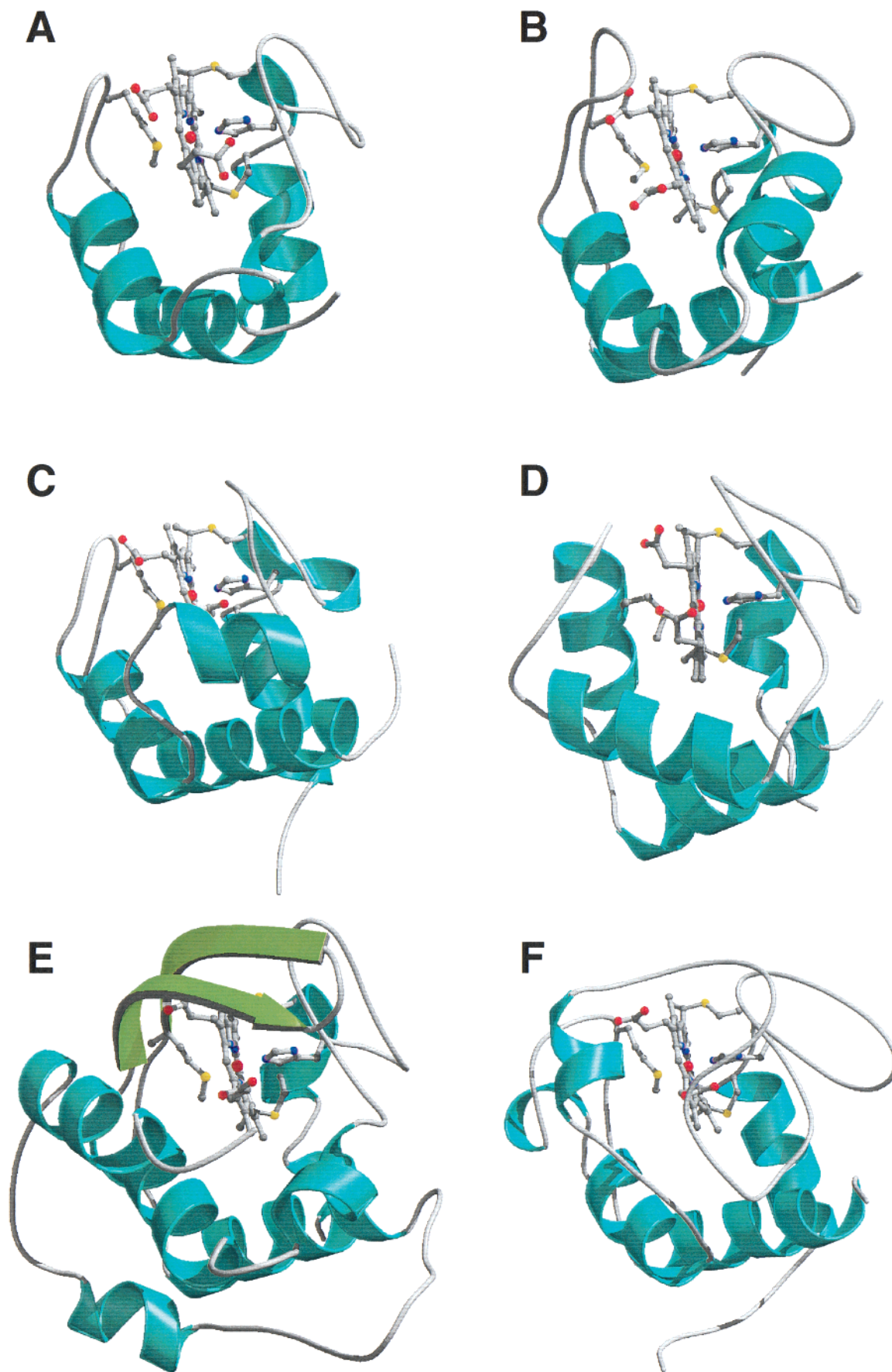
FIGURE 6: "Rogues gallery" of the structurally representative cytochromes picked by DALI. (A) *B. pasteurii* cytochrome *c*$_{553}$; (B) *P. aeruginosa* cytochrome *c*$_{551}$; (C) *M. braunii* cytochrome *c*$_6$; (D) *D. vulgaris* cytochrome *c*$_{553}$; (E) *T. thermophilus* cytochrome *c*$_{552}$; (F) *S. cerevisiae* iso-1 cytochrome *c*. The heme prosthetic groups and the heme coordinating residues are presented as ball-and-stick models colored according to the atom type. The figure was made using BOBSCRIPT (*74*) and rendered with RASTER3D (*75*).

```
B. pasteurii (1B7C)                          V D A E A V V Q Q K - C I S C H G G D L
Ps. aeruginosa (451C)                        E D P E V L F K N K G C V A C H A I D -
M. braunii (1CTJ)                    E A D L A L G K A V F D G N - C A A C H A - G G
D. vulgaris (1C53)                         A D G A A L Y K - S - C V G C H G A D G
T. thermophilus (1C52)                   Q A D G A K I Y A Q - - C A G C H Q Q N G
S. cerevisiae (1YCC)         T E F K A G S A K K G A T L F K T R - C L Q C H T - - V


B. pasteurii (1B7C)          - - - - - T G A - S - A - - P A I D K A G A N Y - - - - - - -
Ps. aeruginosa (451C)        - - - - - T K M - V - G - - P A Y K D V A A K F A G Q A G - -
M. braunii (1CTJ)            - - - - - G N N - V - I P D H T L Q - - K A A I E Q F L D G G
D. vulgaris (1C53)           S - - - K Q A - M - G V G H A V K G Q - - - - - - - - - - - -
T. thermophilus (1C52)       Q - - - G I P G A - F - - P P L A G H V A E I L A K E G - -
S. cerevisiae (1YCC)         E K G G P H K - V - G - - P N L H - - - G I F G R H S G Q A


B. pasteurii (1B7C)          - - - - - - - - - - - - - - - - - - - - S E E E I L D I I L N G Q -
Ps. aeruginosa (451C)        - - - - - - - - - - - - - - - - - - - - A E A E L A Q R I K N G S -
M. braunii (1CTJ)            F - - - - - - - - - - - - - - - - - - - N I E A I V Y Q I E N G K -
D. vulgaris (1C53)           - - - - - - - - - - - - - - - - - - - - K A D E L F K K L K G Y A -
T. thermophilus (1C52)       - - - - - - - - - - - - - - - - - - - - G R E Y L I L V L L Y G L -
S. cerevisiae (1YCC)         E G Y S Y T D A N I K K N V L W D E N N M S E Y L T N P K K


B. pasteurii (1B7C)          - - - - - G - - - - - - - - - - - - G - - M P G G - - I A K
Ps. aeruginosa (451C)        - - - - - Q G V W G P I - - - - - - P - - M P P - - - A V S
M. braunii (1CTJ)            - - - - - G - - - - - - - - - - - - A - - M P A W D G R L D
D. vulgaris (1C53)           - - - - - D G S Y G G E K - - - - - K A V M T N L V K R Y S
T. thermophilus (1C52)       - - - - - Q G Q I E V K G M K Y N G V - - M S S F A - Q L K
S. cerevisiae (1YCC)         Y I P G T K - - - - - - - - - - - - - M A F G G - L K K


B. pasteurii (1B7C)          G A E A E A V A A W L A E K K
Ps. aeruginosa (451C)        D D E A Q T L A K W V L S Q K
M. braunii (1CTJ)            E D E I A G V A A Y V Y D Q A A G N K W
D. vulgaris (1C53)           D E E M K A M A D Y M S K L
T. thermophilus (1C52)       D E E I A A V L N H I A T A W G D A K K V K G F K P F T A E
S. cerevisiae (1YCC)         E K D R N D L I T Y L K K A C E


B. pasteurii (1B7C)
Ps. aeruginosa (451C)
M. braunii (1CTJ)
D. vulgaris (1C53)
T. thermophilus (1C52)       E V K K L R A K K L T P Q Q V L A E R K K L G L K
S. cerevisiae (1YCC)
```
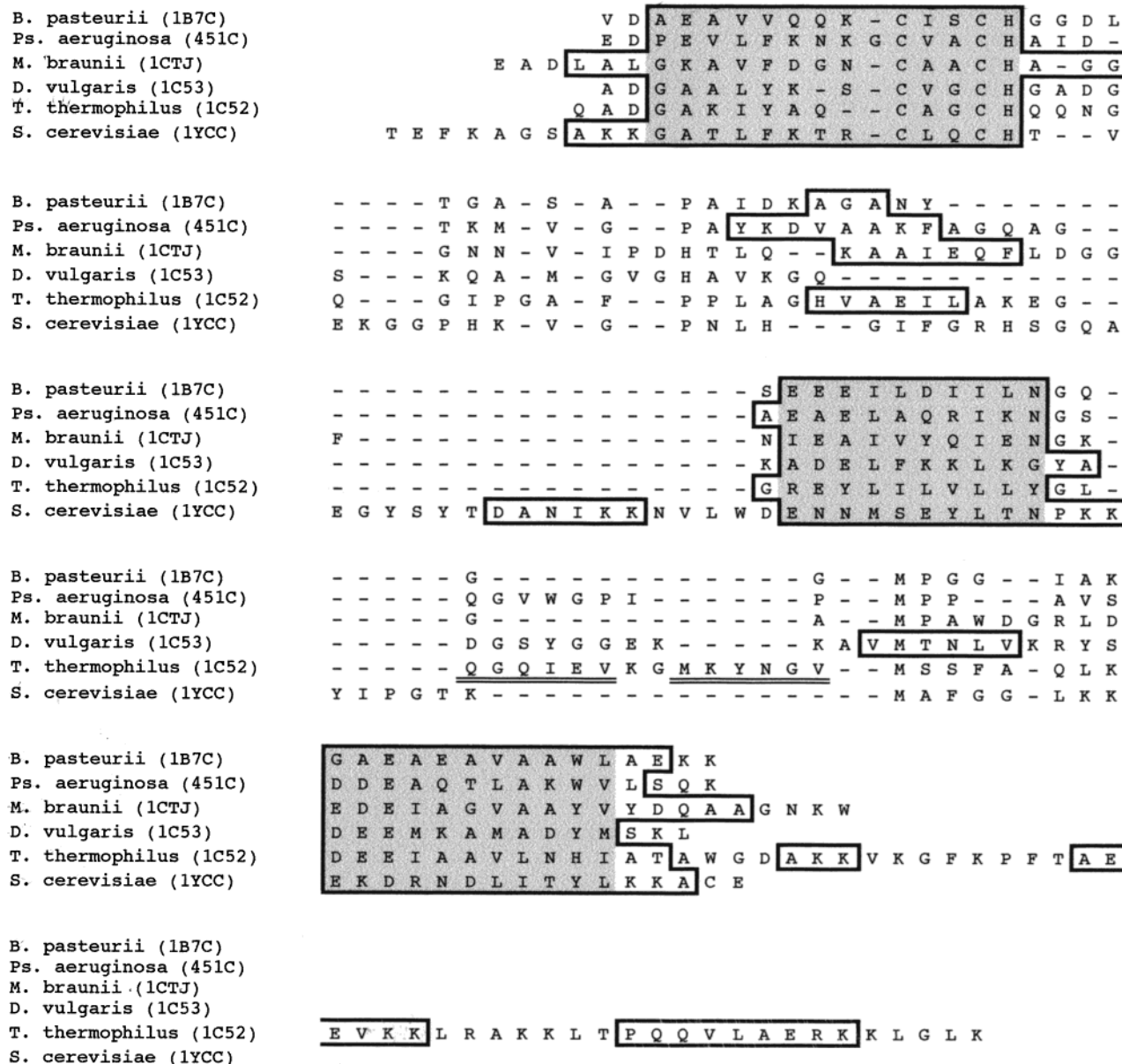
FIGURE 7: Alignment of representative cytochrome sequences based on the superposition of their crystal structure, obtained using DALI (*60*). This figure also displays the secondary structure elements: helices (thick line boxes), β-strands (double underlined). Conserved helices are shaded.

other cytochromes from Gram-positive bacteria such as *Bacillus licheniformis* cytochrome c_{552} (53% identity), thermophilic *Bacillus sp.* PS3 cytochrome c_{551} (45%) and *B. subtilis* cytochrome c_{551} (41%) (*18*). However, a DALI (*60*) search for representative structural analogues in the protein database reveals significant structural similarities between *B. pasteurii* cytochrome c_{553} and, in order, *Pseudomonas* cytochrome c_{551} (Z-score = 9.3), *Monoraphidium braunii* cytochrome c_6 (Z-score = 6.1), *Desulfovibrio vulgaris* cytochrome c_{553} (Z-score = 4.9), *Thermus thermophilus* cytochrome c_{552} (Z-score = 4.7), and *S. cerevisiae* cytochrome c (Z-score = 4.5). These structural analogues have little sequence homology with *B. pasteurii* cytochrome c_{553} (the largest being 32%, relative to *Ps. aeruginosa* cytochrome c_{551}) indicating that the differences in amino acid sequence are not correlated to major tertiary structural modifications.

A visual comparison of the ribbon plot of *B. pasteurii* cytochrome c_{553} shown in Figure 2 with a "rogues gallery" of its structural analogues (Figure 6) reveals that, despite

the remote sequence similarity, the core of conserved helices commonly observed in eukaryotes and Gram-negative bacteria (*61*) is maintained in *B. pasteurii* cytochrome c_{553} and that the presence of various additional sequence fragments characterizes each protein. In particular, the short loop connecting the middle helix and the C-terminus helix in *B. pasteurii* cytochrome c_{553} is replaced by two unique β-strands in *T. thermophilus* cytochrome c_{552}, and by longer extended loops in yeast cytochrome c and *Pseudomonas* cytochrome c_{551}. On the other side of the heme, the Ω-shaped loop connecting the N-terminus and the middle helix in *B. pasteurii* cytochrome c_{553} is replaced by longer extended loops in other organisms. Finally, in cytochrome c_6 a long α-helix is found in the place of the short 3_{10} helix present in *B. pasteurii* cytochrome c_{553}.

A simple amino acid sequence alignment of these distantly related proteins would be difficult because of their very low homology, as determined previously (*18*). However, the observed structural similarities allow the construction of a

Table 5: Heme Accessibility and Redox Parameters for *c*-Type Cytochromes

source	type	PDB code	accessibility (Å²)[a]	$E^{\circ\prime}$ (mV)	$\Delta S^{\circ\prime}$ (J mol⁻¹K⁻¹)[b]	$\Delta H^{\circ\prime}$ (kJ mol⁻¹)[b]
B. pasteurii	c_{553}	1C75	42.0	+47 (*20*)	−163 (*20*)	−53 (*20*)
Ps. aeruginosa	c_{551}	451C	16.5	+276 (*68*)	−134 (*68*)	−66 (*68*)
M. braunii	c_6	1CTJ	19.7	+358 (*76*)	not available	not available
T. thermophilus	c_{552}	1C52	20.1	+230 (*77*)	not available	not available
S. cerevisiae	*c* (iso-1)	1YCC	8.2	+280 (*78*)	−124 (*78*)	−64 (*78*)
horse heart	*c*	1HRC	11.3	+257 (*69*)	−120 (*69*)	−60 (*69*)
Rb. sphaeroides	c_2	1CXC	10.1	+354 (*67*)	−136 (*67*)	−55 (*67*)
Rb. capsulatus	c_2	1C2R	17.9	+347 (*67*)	−133 (*67*)	−52 (*67*)

[a] Total accessibility for the heme group calculated using the SETACC and VACACC subroutines of WHATIF (*36*). The accessibility is defined here as the area traced out by the surface of a water probe sphere having a radius of 1.4 Å. [b] Determined using nonisothermal electrochemical cells.

structure-based alignment using DALI (*60*) (Figure 7). This alignment not only correctly reveals the conservation of residues involved in protein heme binding but also highlights homologous protein fragments that could not have been aligned without structural information. Figure 7 clearly shows that only the common secondary structure elements of *c*-type cytochromes are contained in *B. pasteurii* cytochrome c_{553}.

Electrochemical Reduction Potential and Heme Accessibility. The availability of the structure of *B. pasteurii* cytochrome c_{553} should provide insights into the determinants of the peculiarly low reduction potential observed for this redox protein (+47 mV) (*20*). Such a potential is predominantly determined by a large and negative reduction entropy. The latter was proposed to derive from the extrusion of water molecules from the protein hydration shell into the bulk solvent occurring upon reduction (*20*), on the basis of the compensation theory of biopolymers solvation (*62−64*). This phenomenon, possibly due to the quenching of the positive charge on the heme ring (*65*), was also suggested to occur in eukariotic cytochromes (*66*).

While a positive or negative enthalpic factor is responsible for the relatively *small* reduction potential differences observed for cytochromes belonging to the same structural class (*67*), a negative reduction entropy is invariably observed in cytochromes (*67−69*). This entropy decrease appears to be the major contribution determining the *large* differences in electrochemical reduction potential observed for *c*-type cytochromes belonging to different structural classes (*69*). It has been proposed that such an entropic effect, in addition to differences in solvation properties between the two redox states, is also caused by the increased rigidity of the protein matrix in the reduced form of cytochromes (*15*). This is possibly the result of redox-linked changes in hydrogen bond networks as suggested for cytochrome b_5 (*70*). It is probable that these two hypotheses are actually both valid: the observed higher protein rigidity in reduced cytochromes could be caused by a decrease of water molecules in the hydration shell. This conclusion is supported by recent studies using ¹H nuclear magnetic relaxation dispersion (NMRD) profiles (*71*). These observations suggest a role of the solvent in the regulation of the reduction entropy, and consequently, of the redox properties of the prosthetic heme group. In this context, the heme solvent accessibility has been proposed to play a major role (*55, 69, 72*). However, the molecular basis for such an effect, and in particular the possible influence of heme solvent accessibility on either the reduction enthalpy or entropy, is still unknown.

The existence of some correlation between the heme accessibility and the potential is confirmed by the data reported in Table 5. The cytochromes considered here, for which both the crystal structure and the thermodynamic parameters of the electrochemical reduction have been determined, span a large range of electrochemical properties, with low and high potentials corresponding roughly to small and large solvent accessibility for the heme, respectively. Nevertheless, the linear correlation ($R = 0.79$) is not very satisfactory. A more careful analysis of the data in Table 5 reveals that the heme solvent accessibility correlates much better ($R = 0.93$) with the entropy rather than with the enthalpy ($R = 0.47$) of the reduction. This result suggests a direct link between the major determinant of the electrochemical reduction potential (entropy) to a structural parameter (heme solvent exposure). This conclusion supports the hypothesis that, upon electrochemical reduction of the heme, extrusion of water molecules from the protein hydration shell occurs, affecting a larger number of water molecules in the case of a larger solvent accessibility. This effect would decrease the reduction entropy and, consequently, the reduction potential.

ACKNOWLEDGMENT

REFERENCES

1. Sone, N., and Toh, H. (1994) *FEMS Microbiol. Lett. 122*, 203−210.
2. Jacobs, A. J., Kalra, V. K., Cavari, B., and Brodie, A. F. (1979) *Arch. Biochem. Biophys. 194*, 531−541.
3. Woolley, K. J. (1987) *Arch. Biochem. Biophys. 254*, 376−379.
4. Davidson, M. W., Gray, K. A., Knaff, D. B., and Krulwich, T. A. (1988) *Biochim. Biophys. Acta 933*, 470−477.
5. Sone, N., Kutoh, E., and Yanagita, Y. (1989) *Biochim. Biophys. Acta 977*, 329−334.
6. von Wachenfeldt, C., and Hederstedt, L. (1990) *J. Biol. Chem. 265*, 13939−13948.
7. Hreggvidsson, G. O. (1991) *Biochim. Biophys. Acta 1058*, 52−55.
8. Yumoto, I., Fukumori, Y., and Yamanaka, T. (1991) *J. Biochem. 110*, 267−273.
9. Saraiva, L. M., Denariaz, G., Liu, M.-Y., Payne, W. J., LeGall, J., and Moura, I. (1992) *Eur. J. Biochem. 204*, 1131−1139.
10. Fujiwara, Y., Oka, M., Hamamoto, T., and Sone, N. (1993) *Biochim. Biophys. Acta 1144*, 213−219.
11. Nitschke, W., Schoepp, B., Floss, B., Schricker, A., Rutherford, A. W., and Liebl, U. (1996) *Eur. J. Biochem. 242*, 695−702.
12. Benini, S., Ciurli, S., Rypnjewski, W., and Wilson, K. S. (1997) *Proteins: Struct. Funct. Genet. 28*, 580−585.
13. Albert, I., Rutherford, A. W., Grav, H., Kellermann, J., and Michel, H. (1998) *Biochemistry 37*, 9001−9008.

14. Moore, G. R., and Pettigrew, G. W. (1990) in *Cytochrome c: Evolutionary, Structural and Physicochemical Aspects*, Springer-Verlag, Berlin.

15. Scott, R. A., and Mauk, A. G. (1996) in *Cytochrome c. A Multidisciplinary Approach*, University Science Books, Sausalito, CA.

16. Haddock, B. A., and Cobley, J. G. (1976) *Biochem. Soc. Trans. 4*, 709−711.

17. Hoddinott, M. H., Reid, G. A., and Ingledew, W. J. (1978) *Biochem. Soc. Trans. 6*, 1295−1298.

18. Vandenberghe, I. H. M., Guisez, Y., Ciurli, S., Benini, S., and Van Beeumen, J. J. (1999) *Biochem. Biophys. Res. Commun. 264*, 380−387.

19. Pettigrew, G. W., and Moore, G. R. (1987) in *Cytochromes c: Biological Aspects*, Springer-Verlag, Berlin.

20. Benini, S., Borsari, M., Ciurli, S., Dikiy, A., and Lamborghini, M. (1998) *J. Biol. Inorg. Chem. 3*, 371−382.

21. Hicks, D. B., and Krulwich, T. A. (1995) *Biochim. Biophys. Acta 1229*, 303−314.

22. Benini, S., Gessa, C., and Ciurli, S. (1996) *Soil Biol. Biochem. 28*, 819−821.

23. Matthews, B. W. (1968) *J. Mol. Biol. 33*, 491−497.

24. Gonzàlez, A., Pédelacq, J.-D., Solà, M., Gomis-Ruth, F. X., Coll, M., Samama, J.-P., and Benini, S. (1999) *Acta Crystallogr. D55*, 1449−1458.

25. Dauter, Z. (1997) *Methods Enzymol. 276*, 326−344.

26. Collaborative Computational Project, N. (1994) *Acta Crystallogr. D50*, 760−763.

27. Otwinowski, Z., and Minor, W. (1997) *Methods Enzymol. 276*, 307−325.

28. Jones, T. A., Zou, J. Y., Cowan, S. W., and Kjeldgaard, M. (1991) *Acta Crystallogr. A47*, 110−119.

29. Lamzin, V. S., and Wilson, K. S. (1997) *Methods Enzymol. 277*, 269−305.

30. Murshudov, G. N., Vagin, A. A., and Dodson, E. J. (1997) *Acta Crystallogr. D53*, 240−255.

31. Engh, R. A., and Huber, R. (1991) *Acta Crystallogr. A47*, 392−400.

32. Konnert, J. H. (1976) *Acta Crystallogr. A32*, 614−617.

33. Konnert, J. H., and Hendrickson, W. A. (1980) *Acta Crystallogr. A36*, 344−350.

34. Sheldrick, G. M., and Schneider, T. R. (1997) *Methods Enzymol. 277*, 319−343.

35. Laskowski, R. A., MacArthur, M. W., Moss, D. S., and Thornton, J. M. (1993) *J. Appl. Crystallogr. 26*, 283−291.

36. Vriend, G. (1990) *J. Mol. Graph. 8*, 52−56.

37. Hendrickson, W. A. (1979) *Acta Crystallogr. A35*, 245−247.

38. Fourme, R., Shepard, W., and Khan, R. (1996) *Prog. Biophys. Mol. Biol. 64*, 167−199.

39. Hendrickson, W., and Ogata, C. (1997) *Methods Enzymol. 276*, 494−523.

40. Ogata, C. M. (1998) *Nature Struct. Biol. 5(SS)*, 638−640.

41. Sheldrick, G. (1997) *Methods Enzymol. 276*, 628−641.

42. Kabsch, W., and Sander, C. (1983) *Biopolymers 22*, 2577−2637.

43. Frishman, D., and Argos, P. (1997) *Proteins: Struct., Funct., Gen. 27*, 329−335.

44. Wilson, K. S., Butterworth, S., Dauter, Z., Lamzin, V. S., Walsh, M., Wodak, S., Pontius, J., Richelle, J., Vaguine, A., Sander, C., Hooft, R. W. W., Vriend, G., Thornton, J. M., Laskowski, R. A., MacArthur, M. W., Dodson, E. J., Murshudov, G., Oldfield, T. J., Kaptein, R., and Rullmann, J. A. C. (1998) *J. Mol. Biol. 276*, 417−436.

45. Kerfeld, C. A., Anwar, H. P., Interrante, R., Merchant, S., and Yeates, T. O. (1995) *J. Mol. Biol. 250*, 627−647.

46. Frazao, C., Soares, C. M., Carrondo, M. A., Pohl, E., Dauter, Z., Wilson, K. S., Hervas, M., Navarro, J. A., De la Rosa, M. A., and Sheldrick, G. (1995) *Structure 3*, 1159−1169.

47. Beissinger, M., Sticht, H., Sutter, M., Ejchart, A., Haehnel, W., and Rosch, P. (1998) *EMBO J. 17*, 27−36.

48. Schneckenberg, J., Than, M. E., Mann, K., Wiegand, G., Huber, R., and Reuter, W. (1999) *J. Mol. Biol. 290*, 1019−1030.

49. Than, M. E., Hof, P., Huber, R., Bourenkov, G. P., Bartunik, H. D., Buse, G., and Soulimane, T. (1997) *J. Mol. Biol. 271*, 629−644.

50. Hasegawa, J., Yoshida, T., Yamazaki, T., Sambongi, Y., Yu, Y., Igarashi, Y., Kodama, T., Yamazaki, K., Kyogoku, Y., and Kobayashi, Y. (1998) *Biochemistry 37*, 9641−9649.

51. Allen, J. P., Feher, G., Yeates, T. O., Komiya, H., and Rees, D. C. (1987) *Proc. Natl. Acad. Sci. U.S.A. 84*, 6162−6166.

52. Tiede, D. M., Vashishta, A.-C., and Gunner, M. R. (1993) *Biochemistry 32*, 4515−4531.

53. Meyer, T. E., Bartsch, R. G., Cusanovich, M. A., and Tollin, G. (1993) *Biochemistry 32*, 4719−4726.

54. Davidson, V. L., and Jones, L. H. (1995) *Biochemistry 34*, 1238−1243.

55. Blackledge, M. J., Guerlesquin, F., and Marion, D. (1996) *Proteins: Struct. Funct. Genet. 24*, 178−194.

56. Bushnell, G. W., Louie, G. V., and Brayer, G. D. (1990) *J. Mol. Biol. 214*, 585−595.

57. Luntz, T. L., Schejter, A., Garber, E. A. E., and Margoliash, E. (1989) *Proc. Natl. Acad. Sci. U.S.A. 86*, 3424−3528.

58. Berghuis, A. M., Guillemette, J. G., McLendon, G., Sherman, F., Smith, M., and Brayer, G. D. (1994) *J. Mol. Biol. 236*, 786−799.

59. Lett, C. M., Berghuis, A. M., Frey, H. E., Lepock, E. F., and Guillemette, J. G. (1996) *J. Biol. Chem. 271*, 29088−29093.

60. Holm, L., and Sander, C. (1993) *J. Mol. Biol. 233*, 123−138.

61. Chotia, C., and Lesk, A. M. (1985) *J. Mol. Biol. 182*, 151−158.

62. Lumry, R., and Rajender, S. (1970) *Biopolymers 9*, 1125−1227.

63. Muller, N. (1990) *Acc. Chem. Res. 23*, 23−28.

64. Lee, B., and Graziano, G. (1996) *J. Am. Chem. Soc. 118*, 5163−5168.

65. Cohen, D. S., and Pielak, G. J. (1995) *J. Am. Chem. Soc. 117*, 1675−1677.

66. Margalit, R., and Schejter, A. (1973) *Eur. J. Biochem. 32*, 492−499.

67. Battistuzzi, G., Borsari, M., Sola, M., and Francia, F. (1997) *Biochemistry 36*, 16247−16258.

68. Taniguchi, V. T., Sailasuta-Scott, N., Anson, F. C., and Gray, H. B. (1980) *Pure Appl. Chem. 52*, 2275−2281.

69. Bertrand, P., Mbarki, O., Asso, M., Blanchard, L., Guerlesquen, F., and Tegoni, M. (1995) *Biochemistry 34*, 11071−11079.

70. Dangi, B., Blankman, J. I., Miller, C. J., Volkman, B. F., and Guiles, R. D. (1998) *J. Phys. Chem. 102B*, 8201−8208.

71. Banci, L., Berners-Price, S. J., Bertini, I., Clementi, V., Luchinat, C., Spyroulias, G. A., and Turano, P. (1998) *Mol. Phys. 95*, 797−808.

72. Tezcan, F. A., Winkler, J. R., and Gray, H. B. (1998) *J. Am. Chem. Soc. 120*, 13383−13388.

73. Nicholls, A., Bharadwaj, R., and Honig, B. (1993) *Biophys. J. 64*, A166.

74. Esnouf, B. M. (1997) *J. Mol. Graph. 15*, 133−138.

75. Merritt, E. A., and Bacon, D. J. (1997) *Methods Enzymol. 277*, 505−524.

76. Campos, A. P., Aguiar, A. P., Hervas, M., Regalla, M., Navarro, J. A., Ortega, J. M., Xavier, A. V., De la Rosa, M. A., and Teixeira, M. (1993) *Eur. J. Biochem. 216*, 329−341.

77. Hon-Nami, K., and Oshima, T. (1977) *J. Biochem. (Tokyo) 82*, 769−776.

78. Feinberg, B. A., Petro, L., Hock, G., Qin, W., and Margoliash, E. (1999) *J. Pharm. Biomed. Anal. 19*, 115−125.